

FlexDrive: Toward Trajectory Flexibility in Driving Scene Reconstruction and Rendering

Jingqiu Zhou^{1*} Lue Fan^{1,2,3*} Linjiang Huang⁴
 Xiaoyu Shi¹ Si Liu⁴ Zhaoxiang Zhang^{3†} Hongsheng Li^{1,2†}

¹Multimedia Laboratory, The Chinese University of Hong Kong

²Centre for Perceptual and Interactive Intelligence, Hong Kong

³Institute of Automation, Chinese Academy of Sciences

⁴Beihang University

1155167063@link.cuhk.edu.hk

Abstract

Driving scene reconstruction and rendering have advanced significantly using the 3D Gaussian Splatting. However, most prior research has focused on the rendering quality along a pre-recorded vehicle path and struggles to generalize to out-of-path viewpoints, which is caused by the lack of high-quality supervision in those out-of-path views. To address this issue, we introduce an Inverse View Warping technique to create compact and high-quality images as supervision for the reconstruction of the out-of-path views, enabling high-quality rendering results for those views. For accurate and robust inverse view warping, a depth bootstrap strategy is proposed to obtain on-the-fly dense depth maps during the optimization process, overcoming the sparsity and incompleteness of LiDAR depth data. Our method achieves superior in-path and out-of-path reconstruction and rendering performance on the widely used Waymo Open dataset. In addition, a simulator-based benchmark is proposed to obtain the out-of-path ground truth and quantitatively evaluate the performance of out-of-path rendering, where our method outperforms previous methods by a significant margin.

1. Introduction

3D reconstruction in driving scenes is a cornerstone of a high-quality driving visual simulator. Leveraging NeRF [14] and the emerging 3D Gaussian Splatting [11], the community has made significant progresses [2, 8, 12, 13, 26, 27, 30] in this area, possessing impressive rendering quality in the pre-recorded driving trajectories.

However, a significant issue hinders the current methods from being used in a practical simulator: the rendering quality declines significantly when the viewpoint deviates from the vehicle’s pre-recorded trajectories for data collection. Fig. 1 demonstrates this issue. NeuraD and Street-Gaussian [21, 26] try to solve this problem through building a more accurate geometry, however, their improvements are limited. The essential cause for this issue is the unavailability of ground-truth visual observations from out-of-path viewpoints in driving scenes [1, 7, 18], where only pre-recorded images along a single-pass driving trajectory are available.

To address this issue, UniSim [28] first introduces the concept of lane shift in their driving simulator, where they leverage GAN-generated supervision to refine the rendering quality of out-of-path viewpoints. LidaRF [19] proposed to warp colors from in-path views to the target out-of-path views through the sparse LiDAR points, generating pseudo ground truth of the out-of-path views. However, due to the sparsity of LiDAR points and occlusion in the target view, the pseudo ground truth is usually broken and irregular, having quite different appearances from the real images captured by cameras. These limitations raise a natural question: *can we create a regular and complete pseudo-ground truth for reconstructing the out-of-path views?*

We propose *Inverse View Warping* (IVW) to solve this challenge. Intuitively, IVW is the inverse process of the aforementioned color-warping method. Considering an in-path view A and an adjacent out-of-path view B , all content of A can be captured at viewpoint B if we omit the slight color change and occlusions caused by their different view direction. Inverse View Warping (IVW) tries to render the complete content of A at the viewpoint B , and we use it as the ground truth to reconstruct the out-of-path view B . Specifically, to achieve this warping, we first lift the pixels

*Equal contribution.

†Corresponding author.



Figure 1. We simulate a cut-in case in a high-speed scenario, which is a typical functionality in driving simulators. The representative method PVG [2] fails after the lane change. We provide more video demonstrations in the attached supplementary materials.

of view A into 3D points and then project those points into view B . To render these points from view B , we consider the rays connecting the camera position of B and the projected points. Due to occlusion, trivial alpha-blending can not ensure the rendered colors match their colors at view A , thus we perform *occlusion-aware rasterization* to eliminate the problem of occlusion. Finally, we form a regular image by rearranging the render results in view B with respect to their pixel coordinates in view A , and the resulting regular image should have the same appearance as the in-path counterpart. Thus we can supervise the rearranged rendering results using the in-path counterpart. Unlike basic image warping, which relies on sparse LiDAR, we focus on developing highly accurate dense depth estimation. These precise depth maps enable point-to-point mapping, allowing us to accurately transfer information from the in-path view to the out-of-path view (see Fig. 3). By doing so, we can replace low-quality, trivially warped images—often sparse, distorted, and misaligned—with high-quality recorded ground truth images, facilitating the effective flow and transfer of accurate supervisory signals. Consequently, typical methods such as SSIM, LPIPS, and perceptual loss can be applied.

Since the proposed IVW technique necessitates accurate depth for point lifting, we propose a novel Depth Bootstrap (DB) strategy to generate high-quality depth of the Gaussian field on the fly. We integrate sparse LiDAR points by using our increasingly accurate depth prediction and reduce the inherent LiDAR noise through Linear regression. Utilizing this Depth Bootstrap strategy, we can build dense and accurate depth maps to support the IVW technique. The combination of IVW and DB leads to our overall frame-

work of FlexDrive.

Another hindrance to our goal is the lack of out-of-path ground truth for reliable evaluation. To address this, we turn to driving simulators where free-viewpoint ground truth images can be easily obtained. We build a benchmark based on the popular open-sourced CARLA simulator.

In summary, our contribution comes in four folds:

1. We propose Inverse View Warping, which creates high-quality supervision for out-of-path viewpoints in street scenes, significantly improving reconstruction quality from these novel viewpoints.
2. We propose a novel depth bootstrapping strategy to obtain a dense and accurate depth map, enabling more robust Inverse View Warping.
3. We build a new novel view synthesis benchmark upon the CARLA simulator to evaluate the out-of-path views.
4. In addition to competitive rendering quality in traditional in-path views, our method achieves superior performance in the out-of-path views, validated by quantitative and qualitative results in Waymo dataset and our proposed benchmark.

2. Related Work

3D Gaussian Splatting. 3D Gaussian Splatting (3DGS) [10] have gained significant progress in scene modeling and rendering. While the original 3DGS model focuses on representing static scenes, several researchers have adapted it for dynamic objects and environments. [9, 25, 29] establishes dynamic Gaussian fields by introducing additional neural networks into the point clouds based on 3D Gaussian fields. Another group of re-

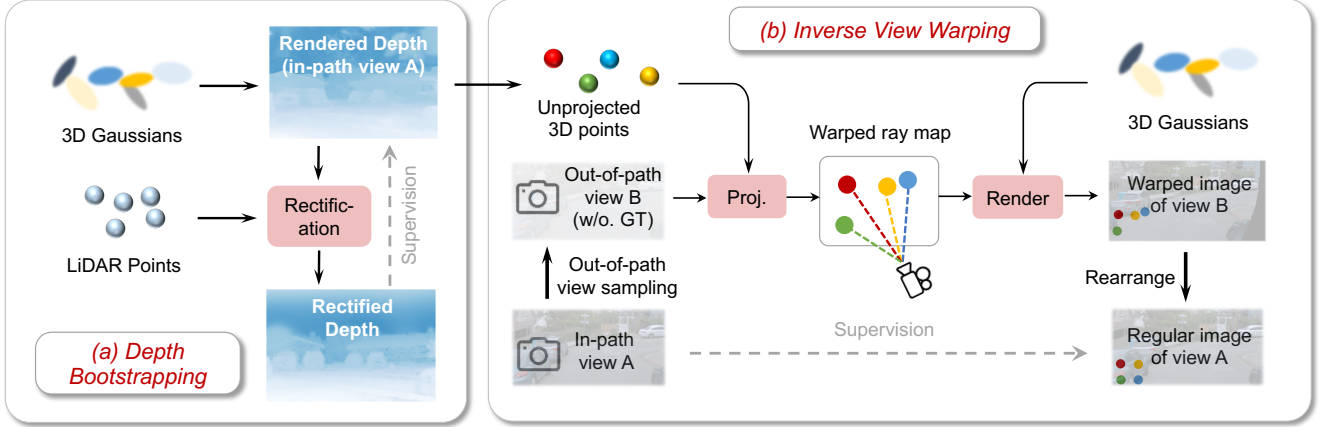


Figure 2. The main framework of FlexDrive, we provide high-quality supervision for out-of-path views through Inverse View Warping technique (IVW). To facilitate IVW, we propose Depth Bootstrapping (DB) to guarantee an accurate and dense depth map.

searchers [26, 30] approaches this problem by developing 3D Gaussian fields which are naturally dynamic. However, the existing approaches are constrained as they can model only the in-path views scenes. Our work extends the reconstruction from in-path views to more flexible rendering locations which truly enables the simulation of autonomous driving tasks.

3DGS in Autonomous Driving Simulation. Great efforts have been made to achieve higher reconstructing quality for autonomous driving scenes. Such reconstruction is essential for creating an autonomous driving environment. Although simulation environments such as CARLA [4], and AirSim [17] exist, they require significant manual effort to create virtual environments and often lack realism in the generated data. A large number of studies have been devoted to this area [3, 6, 12, 13, 15, 16, 20, 21, 23]. These methods primarily concentrate on altering the autonomous driving scene along the data collection trajectory. For example, they can modify the lanes of neighboring cars or remove specific objects. However, simulating an autonomous driving scenario requires more than just these adjustments. The simulation environment must also accommodate maneuvers such as cut-ins, parallel parking, and turns. Achieving this necessitates flexible rendering capabilities, which have not been thoroughly explored in previous research.

3. Method

In this subsection, we first offer an overview of the proposed FlexDrive. Its overall architecture is demonstrated in Fig. 2, which has two major components including Inverse View Warping (IVW, Sec. 3.1) and Depth Bootstrapping (DB, Sec. 3.2). IVW creates high-quality visual supervision for training and improving the rendering at out-of-path virtual viewpoints. Since IVW relies on depth estimation, DB provides accurate and dense depth maps to enhance the

IVW. Furthermore, we also improve dynamic object modeling (Sec. 3.3) to make the FlexDrive better support the reconstruction of dynamic scenes in out-of-path viewpoints. We summarize our optimization objectives in Sec. 3.4.

3.1. Inverse View Warping

Assuming we already have a dense depth (which is later explained in Sec.3.2), our target is to render an in-path view at a randomly sampled out-of-path viewpoint so that we can supervise the out-of-path view with the ground truth in-path camera image. To this end, we propose Inverse View Warping (IVW) to achieve this process. Based on the dense accurate depth acquired through our Depth Bootstrapping strategy, we can accurately convert pixels between viewpoints. The IVW procedure can be decomposed into three steps as shown by Fig. 3. We use \mathcal{V}_{in} to denote the in-path view and \mathcal{V}_{out} to denote a corresponding virtual out-of-path view, which is randomly sampled nearby the \mathcal{V}_{in} .

Warped Ray Map Generation. In this step, we first (lift) the 2D pixel positions from the in-path view \mathcal{V}_{in} back into the 3D space, using the rendered depth map. The obtained 3D points are then projected to the out-of-path view \mathcal{V}_{out} , resulting in a distorted ray map as shown by Fig. 3. Since each ray corresponds to a pixel in \mathcal{V}_{in} , a warped image can also be generated. Using this warped image to supervise the out-of-path view \mathcal{V}_{out} might seem straightforward. However, such a solution is suboptimal as it can introduce incorrect colors due to potential occlusions in \mathcal{V}_{out} . To tackle this challenge, we propose the following Occlusion-aware Rasterization technique.

Occlusion-aware Rasterization. For each ray, we first sort the 3D Gaussian primitives along the ray according to their depth. We then adopt an alpha-blending process within a limited depth range, where the original alpha-blending pro-

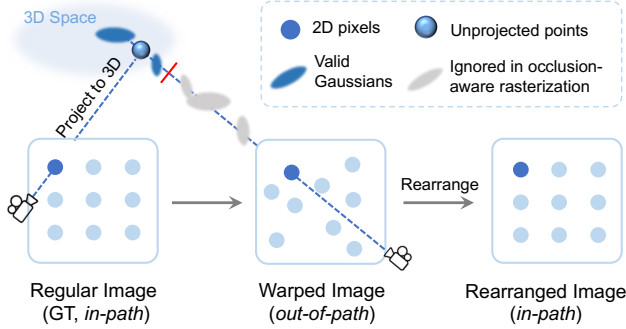


Figure 3. Pipeline for Inverse Views Warping. Firstly, we lift every pixel in the in-path view to 3D space and then project them on a randomly sampled out-of-path view. Our target is to render the original in-path view at this newly sampled location, however, occlusion is inevitable due to the change of view. For this reason, we utilize our Occlusion-aware Rasterization. Finally, we rearrange the rendering points in the out-of-path view according to their pixel coordinates at the in-path view to form a regular image.

cess is modified to

$$C = \sum_{i=1}^N \mathbb{I}(d_i > \beta d_0) \alpha_i \prod_{j=1}^{i-1} (1 - \alpha_j) c_i, \quad (1)$$

where d_i is the depth of the i -th Gaussian primitive and d_0 is the depth of the unprojected point. Eq. (1) indicates that only primitives with a depth larger than βd_0 are involved in the alpha-blending process, illustrated by Fig. 3. Here we introduce β , a coefficient slightly smaller than 1, to take the thickness of Gaussian primitives into account, which avoids mistakenly neglecting the Gaussian primitives near the unprojected 3D points. In this way, even if some regions in \mathcal{V}_{in} are occluded from \mathcal{V}_{out} , we can still provide accurate visual supervision for \mathcal{V}_{out} .

Pixel Rearrangement. The output of occlusion-aware rasterization is a warped image, which has a quite different appearance from the regular image at the in-path view, demonstrated by Fig. 4 (b-c). Thus, we cannot employ the region-level perceptual loss such as SSIM and LPIPS with the warped images. To address this issue, we rearrange the rendered pixels in \mathcal{V}_{out} and recover their relative spatial orders in \mathcal{V}_{in} . In this way, the rendering result in \mathcal{V}_{out} is expected to be the same as the ground truth image in \mathcal{V}_{in} if the Gaussian field is sufficiently optimized, demonstrated by Fig. 4 (d). We then can use the ground truth image in \mathcal{V}_{in} as the supervision for \mathcal{V}_{out} .

Discussion. Considering the original view A and a newly sampled view B , our Warped Ray Map Generation transforms rays from A to B , Occlusion-aware Rasterization then queries colors at B . Finally, we use the Pixel Rearrangement to transform B back to A . Therefore, the in-path view A could provide faithful supervision for the output af-

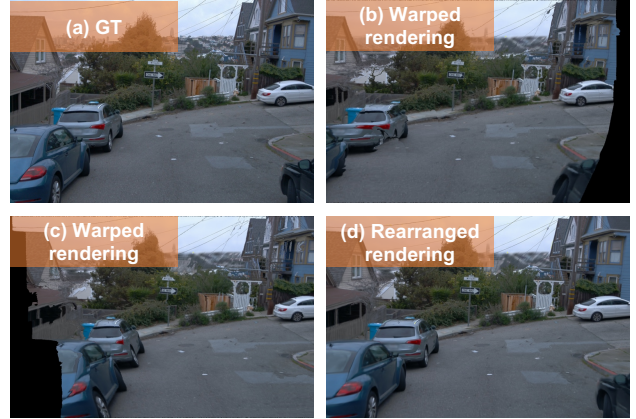


Figure 4. Example of rearrangement. (a) is the ground truth in-path view. (b) and (c) are the warped rendering results in out-of-path views (right and left shifted, respectively). Note we ignore those rendered-pixels out of image boundaries in this illustration. However, in practice, we still keep the out-of-boundary pixels and rearrange them. (d) is the rearranged rendering results in out-of-path views, which is exactly the same as the GT image (a).

ter pixel rearrangement, resembling the cycle-consistency learning [5, 24].

3.2. Depth Bootstrapping

However, the depth information we usually access mainly comes from the sparse LiDAR information, which cannot meet the requirement of IVW. Besides, the sparse depth map can not provide sufficient supervision for the Gaussian Field to build a smooth and continuous depth. What’s more, some degree of noise exists in LiDAR due to inherent error and vehicle vibration. To overcome these issues, we propose a Depth Bootstrapping (DB) strategy. Specifically, we leverage sparse LiDAR information to repeatedly rectify the dense depth map rendered from current reconstructed 3D Gaussians. There are two steps in Depth Bootstrapping: Sparse Depth Initialization and Dense Depth Rectification. The first step accumulates multi-frame LiDAR points and projects them into a training view to initialize the sparse depth map. The second step adopts an efficient linear optimization to minimize the gap between the rendered dense depth map and the sparse depth map.

Sparse Depth Initialization. First, we transform the 3D sparse LiDAR points into the 2D-pixel plane of each in-path training view. For a view at time step t , we first accumulate the 3D LiDAR points in multiple frames (30 frames in our experiments) $[t, t + T]$ into frame t with the provided LiDAR poses. For dynamic objects, we leverage their bounding boxes to move the in-box points to the corresponding positions in frame t . Although this transformation process is straightforward, there are two challenges: (1) Multiple points may be projected to the same image coordinates; (2)

The points of occluded objects could penetrate the occluder due to the sparsity of LiDAR points and be mistakenly projected into the 2D-pixel plane.

To address the two challenges, we propose several simple yet effective rules. Let p_k denote the k -th LiDAR point, and its corresponding image coordinates are denoted as i_k . $\tau(k)$ and $d(k)$ stands for the timestamp and depth of the k -th point, respectively. We then use the following rules to select a subset of these points to build the sparse depth map.

1. If the depth of point i_k deviates from the current rendered depth from 3D Gaussians¹ over a given threshold (e.g., 5% current depth), the point is removed.
2. If point i_{k_1} and point i_{k_2} occupy the same pixel position with $\tau(k_1) < \tau(k_2)$, we keep i_{k_1} and remove i_{k_2} .
3. If point i_{k_1} and point i_{k_2} occupy the same pixel position with depth $d(k_1) < d(k_2)$, we keep i_{k_1} and remove i_{k_2} .

In our rules, we first ensure the LiDAR points are close to the current predicted depth, this rules out points from occlusion. Then close points are preferred than far away because LiDAR point accuracy is highly related to range.

Dense Depth Rectification. Although the sparse depth map is relatively accurate, it only occupies a very small portion of the whole image plane, leading to several problems. (1) The supervision for Gaussian depth is sparse and makes it hard for the Gaussian field to render a smooth and continuous depth map. (2) Floaters, especially floaters in the regions that LiDAR cannot cover, cannot be effectively removed due to a lack of supervision of geometry. (3) More importantly, with a sparse depth map, we can only build sparse visual supervision for the out-of-path viewpoint in the IVW (Sec. 3.1), leading to the imbalance of supervision density.

To tackle these problems, we propose to densify the sparse depth map into a dense one. Our densification process is inspired by the observation that the rendered depth map is highly linear to the sparse depth map built from LiDAR, illustrated in Fig. 5. Thus, we can use the accurate LiDAR depth map as a reference to rectify the rendered depth map by solving a linear optimization problem.

Specifically, given the sparse depth \mathcal{D}_s and the dense rendered depth \mathcal{D}_r , we find the best linear transform parameters that map \mathcal{D}_r to \mathcal{D}_s . Then the rectified rendered depth map can be obtained as:

$$\mathcal{D}'_r = a\mathcal{D}_r + b, \quad (2)$$

where mapping parameters a, b minimize the optimization objective

$$L_{rect} = \sum_i \left\| \frac{a\mathcal{D}_r^i + b - \mathcal{D}_s^i}{\mathcal{D}_s^i} \right\|. \quad (3)$$

¹The Gaussian field is warmed up for 5k iterations and has a relatively good initial depth.

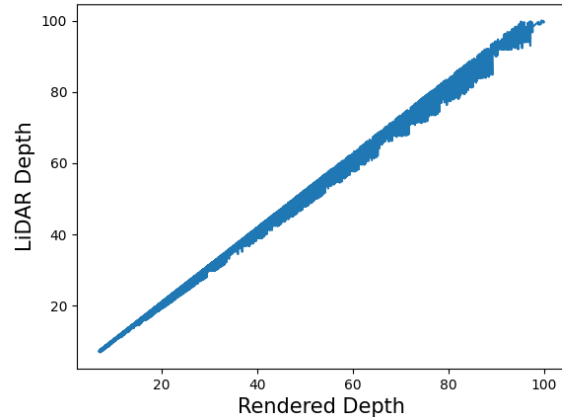


Figure 5. The strong linear prior between LiDAR depth and GS-rendered depth.

Here i indexes the pixel location where sparse LiDAR depth is available. The parameters a and b can be efficiently solved with least squares method. Using the rectified depth \mathcal{D}'_r as supervision, we then optimize the Gaussian field to make its depth more accurate. In this way, we obtain increasingly accurate dense rendered depth maps during the training process.

Discussion. Compared with direct LiDAR depth supervision as in [2, 19], the superiority of our method stems from two aspects: (1) Our method builds a depth map with higher accuracy because only high-confident and reliable sparse depth is leveraged in the sparse map initialization step; (2) We build a dense depth map by utilizing the strong linear prior, demonstrated by Fig. 5, to provide dense supervision for enhancing the supervision density and promoting.

3.3. Constrained Dynamic Object Modeling

Dynamic objects are important components in driving scenarios. Although previous research [9, 26] has made notable success in modeling them at in-path views, we notice that these methods usually result in tailed floaters around the dynamic objects. The tailed floaters severely lower the rendering quality of out-of-path viewpoints. To alleviate this issue, we propose to use a constrained modeling strategy for dynamic objects. Following [26, 30], we represent each dynamic object with a separate 3D Gaussian field. However, different from previous strategies, each dynamic object is constrained in a bounding box in our framework.

Specifically, let (x_o, y_o, z_o) be the logistic coordinates of a Gaussian primitive, we convert them into Euclidean coordinates as follows:

$$\begin{bmatrix} x_t \\ y_t \\ z_t \end{bmatrix} = \begin{bmatrix} l(\sigma(x_o) - 0.5) \\ w(\sigma(y_o) - 0.5) \\ h(\sigma(z_o) - 0.5) \end{bmatrix} \quad (4)$$

The converted Euclidean coordinates are further transformed into the world coordinates by a trainable bounding box pose (details can be found in the supplementary material).

3.4. Loss Functions

RGB Loss. We employ the original RGB loss setting for both in-path views and out-of-path views. They are both supervised by a mixture of L_1 loss and SSIM loss. The overall loss of RGB part can be formulated as

$$L_{RGB} = L_1^{in} + L_1^{out} + \alpha(L_{SSIM}^{in} + L_{SSIM}^{out}), \quad (5)$$

where the superscript *in* and *out* stands for in-path views and out-of-path views.

Depth Loss. We categorize depth supervision into the *near* and *far* regions according to the maximum LiDAR perception range. Let d_i and \hat{d}_i be the depth of i -th pixel in the rendered depth map and the rectified depth map (Eq. (2)), respectively. Then the near-region depth supervision is defined as

$$L_{depth}^{near} = \frac{1}{N_{near}} \sum_{i=1}^{hw} \mathbb{I}(d_i < d_{max}) \left\| \frac{d_i - \hat{d}_i}{\hat{d}_i + \epsilon} \right\|_1, \quad (6)$$

where d_{max} is the maximum LiDAR perception range and N_{near} is the number of near-region pixels in the depth map. For the far-region depth loss L_{depth}^{far} , we directly adopt the ranking loss in [22].

The total loss function can be formulated as:

$$L = \lambda_1 L_{RGB} + \lambda_2 L_{depth}^{near} + \lambda_3 L_{depth}^{far}. \quad (7)$$

4. Experiments

In this section, we evaluate our method on the real-world Waymo dataset and the proposed CARLA-based dataset to accurately evaluate the performance of both in-path setting and out-of-path setting.

4.1. Experiment Setup

Waymo-based in-path Benchmark We first follow the conventional practices [2, 26] to evaluate the performance of the proposed method in the widely used Waymo Open Dataset (WOD). Similar to PVG [2], we conduct our experiments on both dynamic and static split of the Waymo dataset and use the three front cameras. Since there are no ground-truth images of out-of-path views, we mainly focus on the qualitative results for the out-of-path views in the Waymo Open dataset. Additionally, we report FID scores of the out-of-path views as an intuitive but potentially inaccurate quality indicator.

CARLA-based out-of-path Benchmark. In our Waymo experiments, we report FID score between the in-path views

and the out-of-path view, however, this is inaccurate because the distributions between in-path-views and out-of-path views are not necessarily close. To solve this problem, we propose a new benchmark based on the CARLA simulator [4], where the ground-truth images of out-of-path views can be easily obtained. The CARLA-based benchmark is set up with a sensor layout similar to the Waymo dataset. First, a 150-meter range 128-channel LiDAR is mounted on top of the moving vehicle. Furthermore, we mount five cameras on the data-collection vehicle. Three of them are placed on the top of the vehicle to record the in-path training data. The other two cameras are shifted horizontally, which are three meters away from the moving path, to collect the out-of-path ground truth images for evaluation.

Training Scheme. Our training process can be divided into three stages: (1) the warm-up stage, (2) the bootstrapping stage, and (3) the out-of-path training stage. During the warm-up stage, we initialize the 3D Gaussian primitives using multi-frame LiDAR points and conduct training using in-path views without Gaussian densification. Single-frame sparse LiDAR supervision is directly employed in the in-path views, following [2, 19].

In the second stage, we enable the proposed depth bootstrapping and the densification strategy in the original 3DGS. The parameters in the linear transformation (Eq. (2)) are solved by the least squares method.

Finally, we begin the out-of-path training stage. In this stage, we sample an in-path view and randomly generate a nearby out-of-path view for each iteration, as Fig. 2 (b) shows. The rendering results in the in-path view and out-of-path view are supervised by the in-path GT images and pseudo GT image generated in Sec. 3.1. The three stages take 5k, 15k, and 10k iterations, respectively. More configurations of hyper-parameters can be found in the supplementary material.

Compared Methods. In our experiments, we compare our method with both NeRF-based and GS-based baselines. Specifically, we adopt five typical methods for comparison, including EmerNeRF [27], LidaRF [19], NeuraD [21], 3DGS [10], StreetGaussian [26], and PVG [2]. The NeRF-based LidaRF is the most recent state-of-the-art method for out-of-path rendering. However, this method has not been open-sourced, thus we re-implement LidaRF by ourselves. We further transfer the techniques in LidaRF to 3D Gaussian Splatting, resulting in a LidaRF-GS.

4.2. Results on Waymo Dataset

Quantitative Results. We first report the quantitative results in both in-path and out-of-path settings on the Waymo Open dataset. For in-path rendering, conventional metrics PSRN and SSIM are reported. For the out-of-path rendering, we report FID scores as a rough quality indicator since the ground truth images of out-of-path viewpoints are not

Table 1. The performance comparison on the Waymo static and dynamic scenes. We report PSNR and SSIM for the in-path setting and FID for the out-of-path setting. The results are obtained with the default training iterations in the official code.

Model Setting	Year	PSNR \uparrow		SSIM \uparrow		FID@1 meters \downarrow		FID@2 meters \downarrow	
		Static	Dynamic	Static	Dynamic	Static	Dynamic	Static	Dynamic
3D GS [10]	ToG'23	29.40	28.40	0.892	0.869	85.22	100.01	120.34	126.7
PVG [2]	Arxiv'23	30.13	29.77	0.877	0.872	75.97	52.54	99.11	81.76
EmerNeRF [27]	ICLR'24	30.15	28.21	0.828	0.800	65.05	83.53	82.42	106.6
LidaRF [19]	CVPR'24	29.72	30.21	0.889	0.878	69.28	59.26	95.46	83.41
NeuraD [21]	CVPR'24	29.41	29.02	0.854	0.832	57.23	59.55	83.60	84.42
StreetGaussian [26]	ECCV'24	31.35	30.73	0.911	0.883	72.03	78.23	95.34	110.6
FlexDrive (ours)	-	31.25	30.76	0.892	0.886	62.03	58.12	86.05	85.06

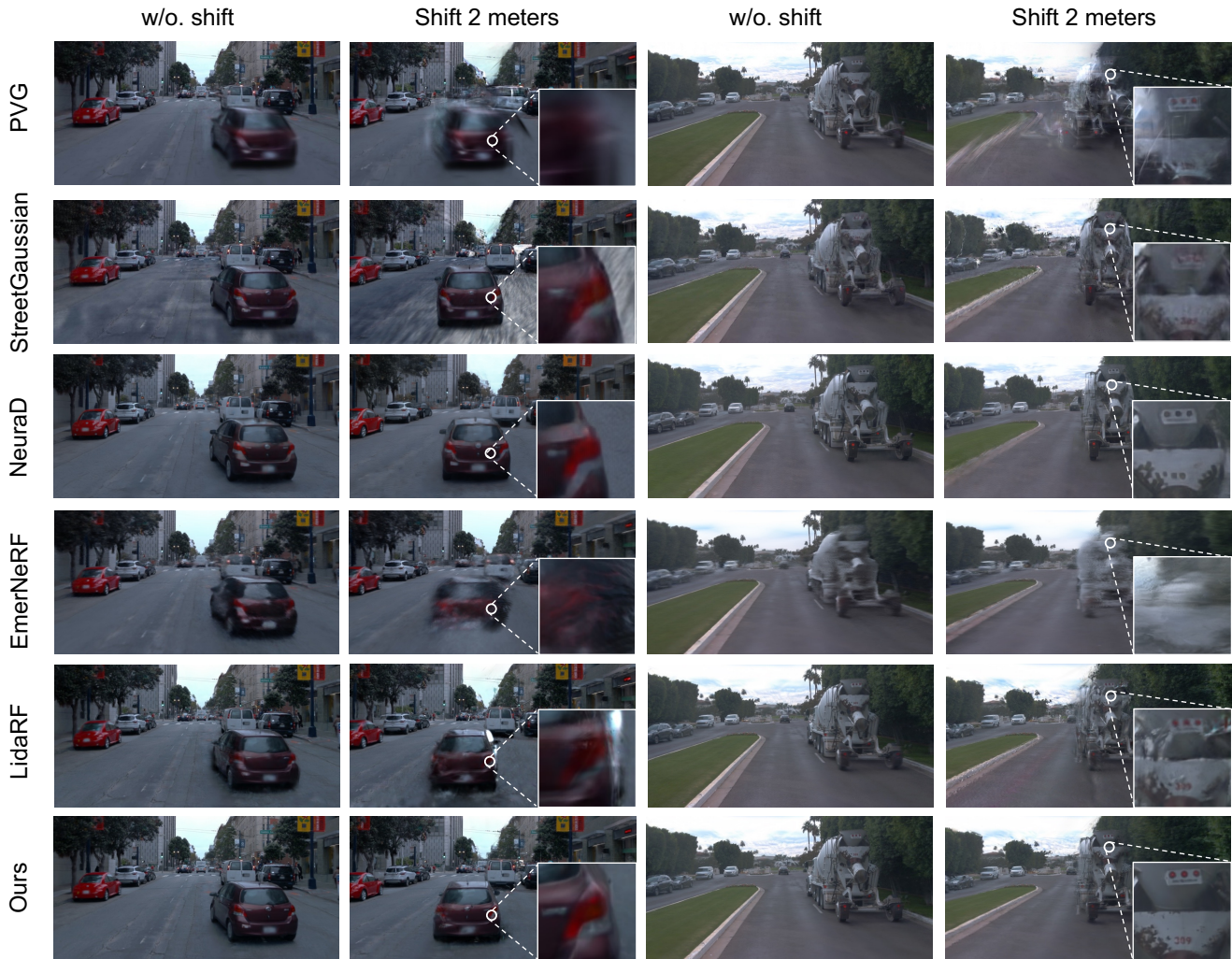


Figure 6. Qualitative comparison. We provide more video demonstrations in the attached supplementary materials.

available. The source distribution used in FID is the in-path ground truth images, and the target distributions are sampled at poses laterally shifted 1 meters and 2 meters away from the vehicle path, respectively. As shown in Table 1, the

proposed FlexDrive achieves comparable performance with the compared methods on the in-path rendering task. When the viewpoints shift away from the in-vehicle path, FlexDrive also achieves relatively good FID scores. However,



Figure 7. The rearranged rendering results in out-of-path views with different β (Eq. (1)). Without the occlusion mechanism ($\beta = 0$), we have incorrect supervision for the out-of-path views.

Table 2. The overall ablation of our proposed techniques. All models are evaluated in the CARLA-based out-of-path setting. The LidaRF-GS is an adaptation of LidaRF [19] to 3DGS, serving as our baseline.

Model Setting	PSNR \uparrow	SSIM \uparrow	LPIPS \downarrow
LidaRF-GS	24.79	0.842	0.410
LidaRF-GS + DB	25.57	0.866	0.381
LidaRF-GS + IVW	25.71	0.876	0.380
LidaRF-GS + DB + IVW (full model)	26.23	0.877	0.372

Table 3. Effectiveness of the occlusion-aware rasterization. $\beta = 0$ means that we do not handle the occlusion problem.

β	PSNR (single scene)
0.95	32.23
0.8	30.90
0.5	29.65
0	20.12

Table 4. CARLA-based out-of-path evaluation. We report the results with the default training iterations in their official code.

Model Setting	PSNR \uparrow	SSIM \uparrow	LPIPS \downarrow
3D GS [10]	18.90	0.701	0.565
EmerNeRF [27]	21.18	0.788	0.463
PVG [2]	21.65	0.753	0.444
LidaRF [19]	24.84	0.852	0.402
NeuraD [21]	25.10	0.863	0.401
StreetGaussian [26]	24.68	0.876	0.411
LidaRF-GS	24.79	0.842	0.410
FlexDrive (ours)	26.23	0.877	0.372

we emphasize that the distribution-based FID score is not a reliable criterion for rendering quality evaluation because it only indicates the overall distribution similarity instead of the detailed rendering quality.

Qualitative Results. We further provide the qualitative results of out-of-path rendering as Fig. 6 shows, where FlexDrive demonstrates significant rendering quality in the out-of-path setting.

4.3. Results on CARLA-based Benchmark

To accurately evaluate the performance on the out-of-path view, we further build a new benchmark upon the CARLA simulator where the ground truth images of out-of-path viewpoints are available. The detailed setting of this benchmark is presented in Sec. 4.1. In Table 4, our method



Figure 8. Effectiveness of Depth Bootstrapping. Depth Bootstrapping provides an effective gradient for the entire Gaussian field. It builds an accurate depth map enabling clearer rendering of objects. Also, it helps to reduce floaters.

largely outperforms the previous street scene reconstruction method in the out-of-path rendering. Notably, FlexDrive achieves a significant performance gain in PSNR compared with LidaRF, which also focuses on the out-of-path setting.

4.4. Ablation Study

In this subsection, we study the impact of each proposed modules. We first conduct an overall ablation for all the proposed modules and then delve into their detailed designs. **Overall Ablation.** We first adopt NeRF-based LidaRF [19] to 3D Gaussian Splatting as our baseline named LidaRF-GS for a step-by-step ablation. We then add the proposed depth bootstrapping and inverse view warping step-by-step to the LidaRF-GS baseline to reveal the performance roadmap. All models are trained with the three stages introduced in Sec. 4.1. We use 400k initial points for all ablation settings. The maximum iteration number is set to 35k. The results

in Table 2 demonstrate that our proposed techniques are all effective and the depth bootstrapping technique indeed enhances the inverse view warping.

Depth Bootstrapping. Depth noise and missing are inevitable in real-world datasets and it may lead to significant errors in the Inverse View Warping module. Fortunately, in FlexDrive, the depth bootstrapping module largely alleviates this issue. Here we use a scene in the real-world Waymo dataset to reveal the efficacy of this module.

Fig. 8 illustrates the rearranged rendering results (similar to Fig. 4 (d)) at out-of-path views with and without depth bootstrapping. As can be seen, DB could effectively enhance the rendering quality, especially for those far regions uncovered by LiDAR. This is because those far regions can also be rectified by Eq. (2).

Occlusion-aware Rasterization in IVW. Occlusion is a key challenge in our inverse view warping strategy. We introduce β to employ a depth range limitation in the alpha-blending process in Eq. (1). Here we study how this parameter impacts the inverse view warping strategy. As shown in Fig. 7, without handling the occlusion ($\beta = 0$), the rearranged results in the out-of-path view are not similar to the in-path ground truth, causing incorrect supervision signals. Such incorrect supervision signals not only reduce the out-of-path rendering quality but also affect the in-path rendering quality since the Gaussian primitives are shared. So we further provide the in-path quantitative results corresponding to Fig. 7, shown in Table 3. The in-path performance has a dramatic drop without depth bootstrapping.

5. Conclusions

In this study, we introduce FlexDrive, featuring the Inverse View Warping and Depth Bootstrap strategy to enhance the reconstruction quality of street scenes, especially from out-of-path viewpoints. Furthermore, we develop a new benchmark using the CARLA simulator for comprehensive evaluation of these views. Our results show that our method not only significantly excels in out-of-path views but also maintains competitive rendering quality in traditional in-path scenarios. We provide both quantitative and qualitative analyses using the Waymo dataset and our CARLA-based benchmark. This advancement paves the way for flexible rendering in reconstructed street scenes. In the future, we plan to combine our method with generative approaches to enable completely free camera movement.

References

- [1] Holger Caesar, Varun Bankiti, Alex H. Lang, Sourabh Vora, Venice Erin Liang, Qiang Xu, Anush Krishnan, Yu Pan, Giancarlo Baldan, and Oscar Beijbom. nuscnets: A multimodal dataset for autonomous driving. *arXiv preprint arXiv:1903.11027*, 2019. 1
- [2] Yurui Chen, Chun Gu, Junzhe Jiang, Xiatian Zhu, and Li Zhang. Periodic vibration gaussian: Dynamic urban scene reconstruction and real-time rendering. *arXiv preprint arXiv:2311.18561*, 2023. 1, 2, 5, 6, 7, 8
- [3] Jie Cheng, Yingbing Chen, Qingwen Zhang, Lu Gan, Chengju Liu, and Ming Liu. Real-time trajectory planning for autonomous driving with gaussian process and incremental refinement. In *2022 International Conference on Robotics and Automation (ICRA)*, pages 8999–9005. IEEE, 2022. 3
- [4] Alexey Dosovitskiy, German Ros, Felipe Codevilla, Antonio Lopez, and Vladlen Koltun. Carla: An open urban driving simulator. In *Conference on robot learning*, pages 1–16. PMLR, 2017. 3, 6
- [5] Debidatta Dwibedi, Yusuf Aytar, Jonathan Tompson, Pierre Sermanet, and Andrew Zisserman. Temporal cycle-consistency learning. In *Proceedings of the IEEE/CVF conference on computer vision and pattern recognition*, pages 1801–1810, 2019. 4
- [6] Lue Fan, Hao Zhang, Qitai Wang, Hongsheng Li, and Zhaoxiang Zhang. Freesim: Toward free-viewpoint camera simulation in driving scenes. *arXiv preprint arXiv:2412.03566*, 2024. 3
- [7] Andreas Geiger, Philip Lenz, Christoph Stiller, and Raquel Urtasun. Vision meets robotics: The kitti dataset. *The International Journal of Robotics Research*, 32(11):1231–1237, 2013. 1
- [8] Jianfei Guo, Nianchen Deng, Xinyang Li, Yeqi Bai, Botian Shi, Chiyu Wang, Chenjing Ding, Dongliang Wang, and Yikang Li. Streetsurf: Extending multi-view implicit surface reconstruction to street views. *arXiv preprint arXiv:2306.04988*, 2023. 1
- [9] Nan Huang, Xiaobao Wei, Wenzhao Zheng, Pengju An, Ming Lu, Wei Zhan, Masayoshi Tomizuka, Kurt Keutzer, and Shanghang Zhang. S3 gaussian: Self-supervised street gaussians for autonomous driving. *arXiv preprint arXiv:2405.20323*, 2024. 2, 5
- [10] Bernhard Kerbl, Georgios Kopanas, Thomas Leimkühler, and George Drettakis. 3d gaussian splatting for real-time radiance field rendering. *ACM Transactions on Graphics*, 42(4), 2023. 2, 6, 7, 8
- [11] Bernhard Kerbl, Georgios Kopanas, Thomas Leimkühler, and George Drettakis. 3d gaussian splatting for real-time radiance field rendering. *ACM Transactions on Graphics*, 42(4), 2023. 1
- [12] Jeffrey Yunfan Liu, Yun Chen, Ze Yang, Jingkang Wang, Sivabalan Manivasagam, and Raquel Urtasun. Real-time neural rasterization for large scenes. In *Proceedings of the IEEE/CVF International Conference on Computer Vision*, pages 8416–8427, 2023. 1, 3
- [13] Fan Lu, Yan Xu, Guang Chen, Hongsheng Li, Kwan-Yee Lin, and Changjun Jiang. Urban radiance field representation with deformable neural mesh primitives. In *Proceedings of the IEEE/CVF International Conference on Computer Vision*, pages 465–476, 2023. 1, 3
- [14] Ben Mildenhall, Pratul P Srinivasan, Matthew Tancik, Jonathan T Barron, Ravi Ramamoorthi, and Ren Ng. Nerf: Representing scenes as neural radiance fields for view syn-

- thesis. *Communications of the ACM*, 65(1):99–106, 2021. 1
- [15] Julian Ost, Fahim Mannan, Nils Thuerey, Julian Knodt, and Felix Heide. Neural scene graphs for dynamic scenes. In *Proceedings of the IEEE/CVF Conference on Computer Vision and Pattern Recognition*, pages 2856–2865, 2021. 3
- [16] Konstantinos Rematas, Andrew Liu, Pratul P Srinivasan, Jonathan T Barron, Andrea Tagliasacchi, Thomas Funkhouser, and Vittorio Ferrari. Urban radiance fields. In *Proceedings of the IEEE/CVF Conference on Computer Vision and Pattern Recognition*, pages 12932–12942, 2022. 3
- [17] Shital Shah, Debadepta Dey, Chris Lovett, and Ashish Kapoor. Airsim: High-fidelity visual and physical simulation for autonomous vehicles. In *Field and Service Robotics: Results of the 11th International Conference*, pages 621–635. Springer, 2018. 3
- [18] Pei Sun, Henrik Kretzschmar, Xerxes Dotiwalla, Aurelien Chouard, Vijaysai Patnaik, Paul Tsui, James Guo, Yin Zhou, Yuning Chai, Benjamin Caine, Vijay Vasudevan, Wei Han, Jiquan Ngiam, Hang Zhao, Aleksei Timofeev, Scott Ettinger, Maxim Krivokon, Amy Gao, Aditya Joshi, Yu Zhang, Jonathon Shlens, Zhifeng Chen, and Dragomir Anguelov. Scalability in perception for autonomous driving: Waymo open dataset. In *Proceedings of the IEEE/CVF Conference on Computer Vision and Pattern Recognition (CVPR)*, 2020. 1
- [19] Shanlin Sun, Bingbing Zhuang, Ziyu Jiang, Buyu Liu, Xiaohui Xie, and Manmohan Chandraker. Lidarf: Delving into lidar for neural radiance field on street scenes. In *Proceedings of the IEEE/CVF Conference on Computer Vision and Pattern Recognition*, pages 19563–19572, 2024. 1, 5, 6, 7, 8
- [20] Matthew Tancik, Vincent Casser, Xinchun Yan, Sabeek Pradhan, Ben Mildenhall, Pratul P Srinivasan, Jonathan T Barron, and Henrik Kretzschmar. Block-nerf: Scalable large scene neural view synthesis. In *Proceedings of the IEEE/CVF Conference on Computer Vision and Pattern Recognition*, pages 8248–8258, 2022. 3
- [21] Adam Tonderski, Carl Lindström, Georg Hess, William Ljungbergh, Lennart Svensson, and Christoffer Petersson. Neurad: Neural rendering for autonomous driving. In *Proceedings of the IEEE/CVF Conference on Computer Vision and Pattern Recognition*, pages 14895–14904, 2024. 1, 3, 6, 7, 8
- [22] Guangcong Wang, Zhaoxi Chen, Chen Change Loy, and Ziwei Liu. Sparsenerf: Distilling depth ranking for few-shot novel view synthesis. In *Proceedings of the IEEE/CVF International Conference on Computer Vision*, pages 9065–9076, 2023. 6
- [23] Qitai Wang, Lue Fan, Yuqi Wang, Yuntao Chen, and Zhaoxiang Zhang. Freevs: Generative view synthesis on free driving trajectory. *arXiv preprint arXiv:2410.18079*, 2024. 3
- [24] Xiaolong Wang, Allan Jabri, and Alexei A Efros. Learning correspondence from the cycle-consistency of time. In *Proceedings of the IEEE/CVF conference on computer vision and pattern recognition*, pages 2566–2576, 2019. 4
- [25] Guanjun Wu, Taoran Yi, Jiemin Fang, Lingxi Xie, Xiaopeng Zhang, Wei Wei, Wenyu Liu, Qi Tian, and Xinggang Wang. 4d gaussian splatting for real-time dynamic scene rendering. In *Proceedings of the IEEE/CVF Conference on Computer Vision and Pattern Recognition*, pages 20310–20320, 2024. 2
- [26] Yunzhi Yan, Haotong Lin, Chenxu Zhou, Weijie Wang, Haiyang Sun, Kun Zhan, Xianpeng Lang, Xiaowei Zhou, and Sida Peng. Street gaussians: Modeling dynamic urban scenes with gaussian splatting. In *ECCV*, 2024. 1, 3, 5, 6, 7, 8
- [27] Jiawei Yang, Boris Ivanovic, Or Litany, Xinshuo Weng, Seung Wook Kim, Boyi Li, Tong Che, Danfei Xu, Sanja Fidler, Marco Pavone, et al. Emernerf: Emergent spatial-temporal scene decomposition via self-supervision. In *ICLR*, 2024. 1, 6, 7, 8
- [28] Ze Yang, Yun Chen, Jingkang Wang, Sivabalan Manivasagam, Wei-Chiu Ma, Anqi Joyce Yang, and Raquel Urtasun. Unisim: A neural closed-loop sensor simulator. In *Proceedings of the IEEE/CVF Conference on Computer Vision and Pattern Recognition*, pages 1389–1399, 2023. 1
- [29] Ziyi Yang, Xinyu Gao, Wen Zhou, Shaohui Jiao, Yuqing Zhang, and Xiaogang Jin. Deformable 3d gaussians for high-fidelity monocular dynamic scene reconstruction. In *Proceedings of the IEEE/CVF Conference on Computer Vision and Pattern Recognition*, pages 20331–20341, 2024. 2
- [30] Xiaoyu Zhou, Zhiwei Lin, Xiaojun Shan, Yongtao Wang, Deqing Sun, and Ming-Hsuan Yang. Drivinggaussian: Composite gaussian splatting for surrounding dynamic autonomous driving scenes. In *Proceedings of the IEEE/CVF Conference on Computer Vision and Pattern Recognition*, pages 21634–21643, 2024. 1, 3, 5